Adsorption of Ar into zeolite Al-MFI (NH_4)

Colin W. Scherry,[1] James A. Kaduk,[1,2,a)] Winnie Wong-Ng,[3] and Huong Giang T. Nguyen[4]
[1]*North Central College, 131 S. Loomis St., Naperville, IL 60540, USA*
[2]*Illinois Institute of Technology, 3101 S. Dearborn St., Chicago, IL 60616, USA*
[3]*Materials Measurement Science Division, National Institute of Standards and Technology, Gaithersburg, MD 20899-8520, USA*
[4]*Chemical Sciences Division, National Institute of Standards and Technology, Gaithersburg, MD, 20899-8390, USA*

(Received 22 July 2023; accepted 19 November 2023)

The crystal structure of anhydrous Al-MFI (NH_4) containing adsorbed Ar has been determined and refined using synchrotron X-ray powder diffraction data taken at 90 K, and optimized using density functional theory techniques. Six highly occupied Ar sites almost completely fill the pore volume of the zeolite. Changing the gas flow from Ar to He at 90 K decreases the Ar occupancies of all six sites, but two decrease more than the others. Warming the sample from 90 to 295 K in Ar flow results in further decreases in site occupancies, but five of the original six sites persist.

[doi:10.1017/S0885715623000453]

Keywords: MFI, zeolite, argon, Rietveld refinement, density functional theory

I. INTRODUCTION

To mitigate global warming as a result of fossil fuel burning, CO_2 capture and storage (CCS) technology is critical. The development of novel solid sorbent materials could provide an economical way to capture CO_2. As extensive research work has been carried out in recent years on solid sorbent materials, standard reference materials are critical for the CO_2 capture research community for adsorption characterization. At the National Institute of Standards and Technology (NIST), we have been investigating potential reference materials as gas adsorption standards (Nguyen et al., 2018, 2022). One of the candidate materials is ZSM-5, which is an aluminosilicate zeolite with framework type MFI. The general structure of ZSM-5 is shown in Figure 1, which shows a three-dimensional network of 10-ring pores straight along the *b*-axis, and zig-zag pores along the *a*-axis. The general formula of this material is $(NH_4)_nAl_nSi_{96-n}O_{192}(H_2O)_x$ $(0 < n < 27)$. Our sample has $n = 3.27$, resulting in a formula of $(NH_4)_{3.27}Al_{3.27}Si_{92.73}O_{192}(H_2O)_{26.7}$.

Argon adsorption in zeolites has been studied, but not extensively. Adsorbed Ar in zeolite LTA has been characterized by Heo et al. (1996; Powder Diffraction File entries 01-089-0452 and 0453, 04-009-1947 and 1948), in FAU by Guesmi et al. (2012; PDF entry 01-081-8367), and in NAT by Lee et al. (2010; PDF entry 01-079-6137). In LTA and NAT, the Ar was adsorbed at high pressure ($\approx 3 \times 10^3$ MPa). For FAU, the Ar adsorption experiments were done at 295 K and 0.1 MPa; the zeolite was K-LSX, hence there was a high concentration of cations.

It has been reported by Cho et al. (2012) that for MFI with only Si content (no Al), a clear peak (or step increase) appears at the Ar adsorption curve at an Ar pressure between 10 and 200 Pa (or between 0.0001 and 0.002 bar) at 83 K. This appearance of a peak agrees with phase transition pressure by *in situ* synchrotron diffraction studies at around 126 Pa. They concluded that the step increase in the Ar adsorption isotherm is due to the phase transition of the zeolite from monoclinic ($P2_1/n$) at low pressure to orthorhombic (*Pnma*) at higher pressure. Phase transformation often has a great impact on the sorption process.

$(NH_4)_{3.27}Al_{3.27}Si_{92.73}O_{192}(H_2O)_{26.7}$ shows an extremely small step at a similar Ar pressure as reported by Cho et al. (2012). But the small peak was absent at the desorption portion of the curve. There has been much disagreement as to the origin of this peak. We had anticipated to characterize the structure of MFI containing adsorbed Ar as a function of pressure, but at the time of this work, the gas handling capabilities of beamline 11-BM at advanced photon source (APS) were relatively limited (they have since been improved).

As the structures of NH_4-MFI with and without Ar have not been reported, the structural results are expected to demonstrate whether phase transformation takes place; and if it does, whether it is a reversible one. The locations of Ar atoms corresponding to the Ar pressure are also important to understand the adsorption mechanism.

II. EXPERIMENTAL

A. Materials synthesis and preliminary characterization

The ZSM-5 zeolite studied here is a reference material (RM 8852™, formula $(NH_4)_{3.27}Al_{3.27}Si_{92.73}O_{192}(H_2O)_{26.7}$) obtainable from NIST. This zeolite was donated by a major zeolite manufacturer. The sample has been characterized by a variety of chemical and physical measurement techniques (Turner et al., 2008), including X-ray fluorescence (XRF), gravimetry, instrumental neutron activation analysis (INAA), nuclear magnetic resonance (NMR), calorimetry, synchrotron X-ray diffraction, neutron diffraction, laser light extinction, laser light scattering, electric sensing zone, X-ray sedimentation, scanning transmission electron microscopy (STEM),

a)Author to whom correspondence should be addressed. Electronic mail: kaduk@polycrystallography.com

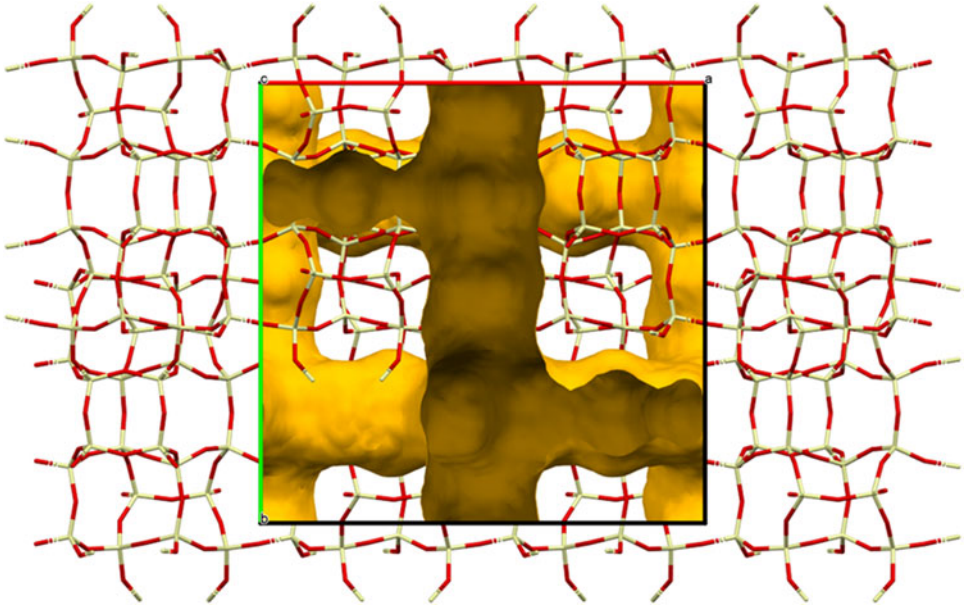

Figure 1. The crystal structure of zeolite MFI as viewed down the orthorhombic *c*-axis. Si atoms are colored tan, and O atoms are red. The yellow surface indicates the pores, with a probe radius of 1.2 Å. The straight channels (vertical) lie parallel to the *b*-axis, and the zig-zag channels (horizontal) join them along the *a*-axis. Image generated using Mercury (Macrae et al., 2020).

scanning electron microscopy (SEM), and optical microscopy. Reference values are given for the major components (major elements, loss on ignition [LOI] and loss on fusion [LOF]), trace elements, and Si/Al and Na/Al ratios. Information values are given for enthalpies of formation, unit cell parameters, particle size distributions, refractive indices, and variation of mass with variation in relative humidity (RH). Readers are referred to the reference by Turner et al. (2008) for details.

B. X-ray diffraction characterization

The white powder of RM8852, $(NH_4)_{3.27}Al_{3.27}Si_{92.73}O_{192}(H_2O)_{26.7}$, was packed into a 1.1 mm diameter Kapton capillary, and mounted in a gas flow cell. The powder patterns were measured at beam line 11-BM (Antao et al., 2008; Lee et al., 2008; Wang et al., 2008) of the Advanced Photon Source at Argonne National Laboratory using a wavelength of 0.412689(2) Å from 0.5 to 34.0° 2θ with a step size of 0.001° and a counting time of 0.1 s/step. The high-resolution powder diffraction data were collected using 12 silicon crystal analyzers that allow for high angular resolution, high precision, and accurate peak positions. A mixture of silicon (NIST SRM 640c) and alumina (NIST SRM 676a) standards (ratio Al_2O_3:Si = 2:1 by mass) was used to calibrate the instrument and refine the monochromatic wavelength used in the experiment.

A preliminary pattern (11bmb_8189) was measured at ambient conditions (292 K). The temperature of the Oxford Cryostream (The purpose of identifying the equipment and software in this article is to specify the experimental procedure. Such identification does not imply recommendation or endorsement by the National Institute of Standards and Technology) was set to 420 K and the sample was heated at 6 K/min under a flow of He at ≈5 mL/min. The intent was to be high enough to dehydrate and activate the sample but not decompose the ammonium cations. A pattern was measured at the end of the temperature ramp from 325 to 420 K (11bmb_8190). The Cryostream was then set to 90 K, and the sample was cooled under He flow. A pattern was measured at 95(5) K during the end of the cooling period (11bmb_8191). The gas flow was then switched to Ar at ≈5 mL/min. Three patterns were measured at 90(1) K under Ar flow (8192-8194). The gas flow was switched to He, and 12 patterns (11bmb_8195-11bmb_8206) were measured overnight. The gas was switched to Ar, and the sample was heated to 295 K. A final pattern (11bmb_8207) was measured under Ar flow at 295 K.

Rietveld refinements were carried out using GSAS-II (Toby and Von Dreele, 2013). Only the 1.8°–27.0° portion of the pattern was included in the refinement (d_{min} = 0.884 Å). For orthorhombic MFI, the initial structure model was an unpublished one developed by JAK during his time at Amoco. For the monoclinic structure at 90 K, the initial model was taken from Artioli et al. (2000). The tetrahedral sites were described as 100% Si. All Si–O bond distances were restrained to 1.62(1) Å, all O–Si–O angles to 109.5 (30)°, and Si–O–Si angles to 145(5)°. The restraints contributed ≈12% to the final χ^2, mostly from the angle restraints. The U_{iso} were grouped by atom type. When U_{iso} refined to (slightly) negative values, they were fixed at reasonable values. The peak profiles were described using the generalized microstrain model (Stephens, 1999). The background was modeled using a three-term shifted Chebyshev polynomial, and a peak around 6.1° 2θ to model the scattering from the Kapton capillary and any amorphous component.

The final refinement residuals are summarized in Table I. A representative Rietveld plot is shown in Figure 2. The largest errors in the difference plot (Figure 2) are in the shapes of the lowest-angle peaks.

The structure of Ar-MFI was optimized (fixed experimental unit cell) with density functional techniques using VASP (Kresse and Furthmüller, 1996) through the MedeA graphical interface (Materials Design, 2016). Two cases were explored: (1) all Ar sites fully occupied, and (2) each Ar site individually fully occupied (six separate optimizations). The calculations

https://doi.org/10.1017/S0885715623000453 Published online by Cambridge University Press

TABLE I. Refinement residuals for Ar-MFI study.

Run 11bmb_	T (K)	Gas	R_{wp}	GOF	% χ^2 from restr.	$\Delta F, +(e\text{Å}^{-1})$	$\Delta F, -(e\text{Å}^{-1})$
8189	295	Air	0.1360	2.70	12.6	0.92(17)	−0.66(17)
8190	420	He	0.1233	2.58	10.4	0.81(13)	−0.57(13)
8191	95(5)	He	0.1143	3.23	12.6	0.87(18)	−0.70(18)
8192	90	Ar	0.0734	2.11	14.3	0.59(13)	−0.60(13)
8193	90	Ar	0.0730	2.09	14.6	0.58(13)	−0.58(13)
8194	90	Ar	0.1013	2.09	14.9	0.57(13)	−0.61(13)
8195	90	He	0.0722	2.06	15.3	0.57(13)	−0.61(13)
8196	90	He	0.0995	2.16	12.1	0.61(13)	−0.53(12)
8197	90	He	0.0992	2.14	11.6	0.61(14)	−0.56(14)
8198	90	He	0.1014	2.16	12.5	0.68(15)	−0.68(15)
8199	90	He	0.1016	2.15	12.4	0.70(15)	−0.68(15)
8200	90	He	0.1012	2.16	12.2	0.74(15)	−0.70(15)
8201	90	He	0.1019	2.18	12.4	0.73(15)	−0.70(15)
8202	90	He	0.1015	2.17	12.7	0.73(15)	−0.70(15)
8203	90	He	0.1019	2.16	12.7	0.77(15)	−0.69(15)
8204	90	He	0.1015	2.17	12.8	0.69(15)	−0.69(15)
8205	90	He	0.1015	2.17	12.8	0.76(16)	−0.72(15)
8206	90	He	0.1011	2.17	13.1	0.72(15)	−0.70(15)
8207	295	Ar	0.0862	2.41	12.0	0.54(13)	−0.60(13)

Values inside brackets represent standard deviations.
$\Delta F+$ is the magnitude of the largest peak in a difference Fourier map, and $\Delta F-$ is the magnitude of the deepest hole in the map.

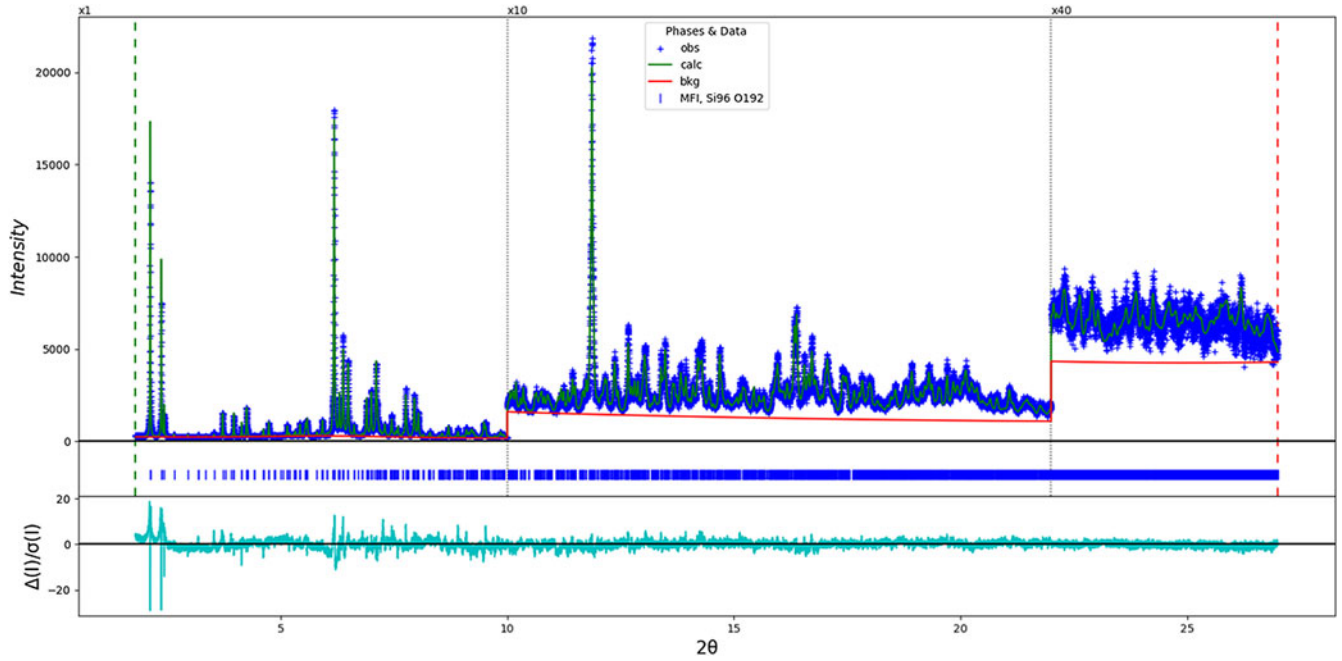

Figure 2. The Rietveld plot for the refinement of Al-MFI (Ar), using dataset 11bmb_8192. The blue crosses represent the observed data points, and the green line is the calculated pattern. The cyan curve is the normalized error plot, and the red line is the background curve. The vertical scale has been multiplied by a factor of 10× for $2\theta > 10.0°$, and by a factor of 40× for $2\theta > 22.0°$.

were carried out on 16 2.4 GHz processors (each with 4 Gb RAM) of a 64-processor HP Proliant DL580 Generation 7 Linux cluster at North Central College. The calculation used the GGA-PBE functional, a plane wave cutoff energy of 400.0 eV, and a k-point spacing of 0.5 Å^{-1} leading to a 1 × 1 × 1 mesh, and took ≈15 h each.

III. RESULTS AND DISCUSSION

The raw patterns change with temperature and gas, so the structure changes significantly with changes in the environment (Figure 3). A difference Fourier map using the framework-only structure at ambient conditions yielded a peak on the mirror plane perpendicular to the b-axis. This peak was assigned to the N atom of an ammonium cation, and H atoms were included and refined. Both the N–H distances (1.012 Å) and H–N–H angles (109.5°) were restrained. As expected, the occupancy of the ammonium cation and the displacement coefficients were highly correlated. Refinements of these quantities separately suggested high occupancy with reasonable displacement coefficients, so in the final refinement, the ammonium occupancy was fixed at 1.0. This results in 4 ammonium ions/cell, larger than the expected value of 3.27. (Perhaps this site is also partially occupied by water

https://doi.org/10.1017/S0885715623000453 Published online by Cambridge University Press

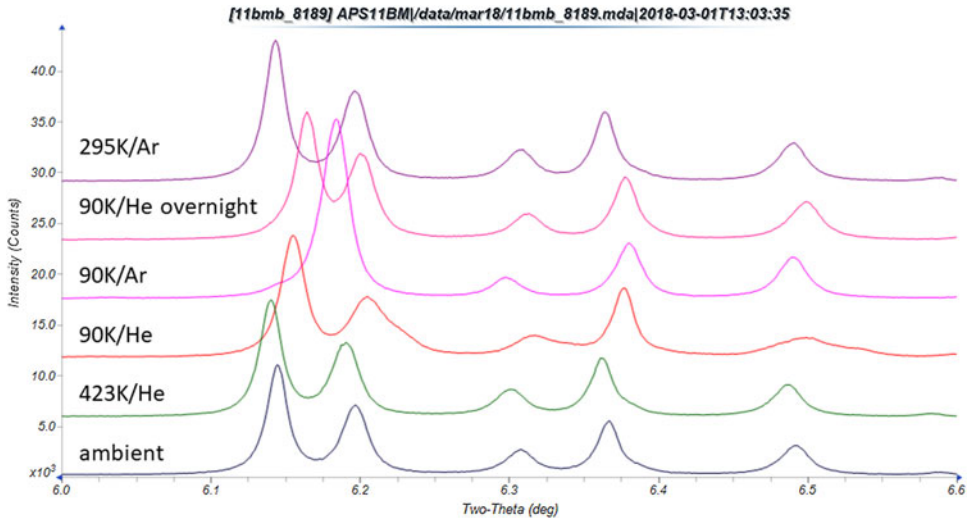

Figure 3. Changes in a small portion of the X-ray powder diffraction pattern of MFI as a function of temperature and atmosphere. Image generated using JADE Pro (MDI, 2023).

molecules). The ammonium cation lies in the zig-zag channels, between the straight channels (Figure 4). The ammonium ion does not seem to hydrogen bond to the framework; the shortest N···O distances are 3.774 Å (to O33), and 3.805 Å (to two different O20). As is typical at ambient conditions, the water molecules are so disordered that they cannot be located.

At 423 K, the orthorhombic unit cell volume increases by 0.26% compared to ambient conditions (Figure 5). The expansion is slightly larger in the *a*- and *b*-directions (0.11%) than in the *c*-direction (0.07%). The ammonium ion remained in the same site, and fully occupied. No other extraframework sites could be refined.

On cooling to 90 K in flowing He, the symmetry was lowered to monoclinic, and the unit cell volume decreased by 0.56% compared to ambient conditions. The ammonium ion remained in a similar site, but its refined occupancy was somewhat greater than unity and was reset to 1.0.

Changing the gas flow from He to Ar at 90 K resulted in a change of symmetry back to orthorhombic, and lattice expansion (Figure 5). Difference Fourier maps indicated the population of six extraframework sites (Ar39–Ar44). The original site of the ammonium cation lies between Ar40 and Ar42. All of the extraframework sites were modeled as partially occupied Ar atoms. It is possible that some of the sites are also partially occupied by He atoms, but their detection is beyond the sensitivity of this experiment. We likewise did not attempt to model the ammonium ion after Ar had been adsorbed. The refined site occupancies were high and varied from 0.75 to 1.00.

The Ar atoms basically fill both the straight and zig-zag channels (Figures 6 and 7). The site occupancies correspond to 29 Ar/cell, compared to the maximum of 32 Ar/cell from the site multiplicities. The van der Waals radius of Ar is 1.88 Å, and that of O is 1.4 Å. The interaction of the Ar atoms among themselves and the framework thus seem to

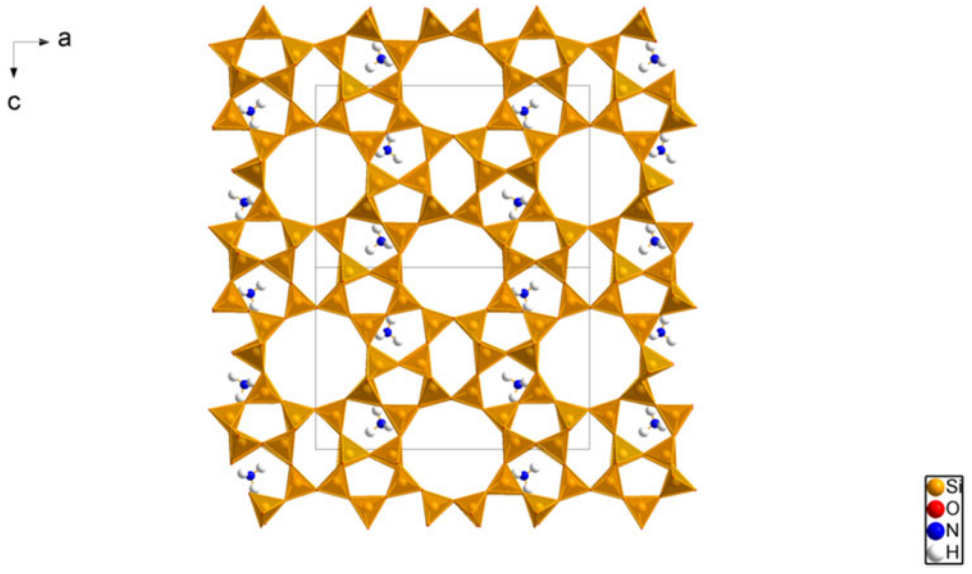

Figure 4. The crystal structure of Al-MFI (NH_4) is viewed down the *b*-axis. The straight channels are parallel to the *b*-axis, and the zig-zag channels are parallel to the *a*-axis. Image generated using Diamond (Crystal Impact, 2022).

https://doi.org/10.1017/S0885715623000453 Published online by Cambridge University Press

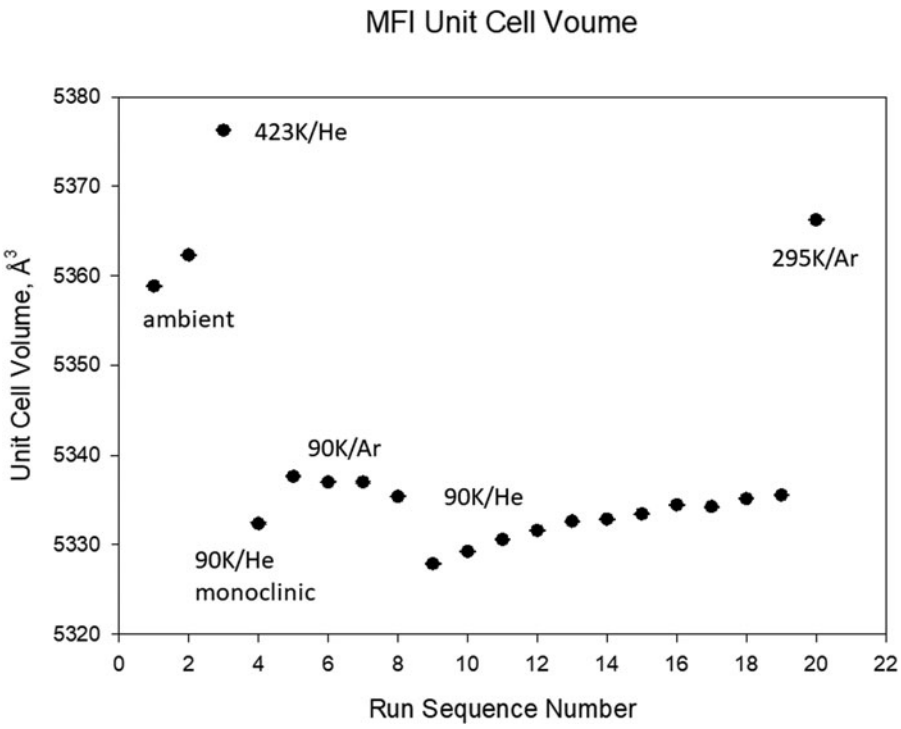

Figure 5. Changes in the unit cell volume of MFI as a function of temperature and atmosphere.

be van der Waals interactions (Table II). The Ar–O distances are comparable to those in NAT (2.9–3.3 Å) and LTA (3.6–3.9 Å).

A single-point energy calculation and population analysis using CRYSTAL23 (Erba et al., 2023) indicated that the charges on the Si atoms were +2.0, the O atoms −1.0, and the Ar atoms 0.0. The Mulliken overlap populations in the Si–O bonds ranged from 0.25 to 0.30 *e*, indicating that these bonds have significant covalent character. The overlap populations did not reveal any directional interactions between the Ar atoms and the framework. The Density of States calculated using VASP indicated that the highest-energy-occupied bands consist of O *p* states. The Ar *p* states occupy a band 2–4 eV below the Fermi level.

The root-mean-square Cartesian displacement of the Si atoms (8192) between the Rietveld-refined and DFT-optimized structures is 0.128 Å. That for the O is 0.191 Å, and for the Ar is 0.170 Å. These are well within the normal range for correct structures (van de Streek and Neumann, 2014).

On changing the gas flow from Ar to He at 90 K, the occupancies of all six Ar sites decreased and equilibrated in about

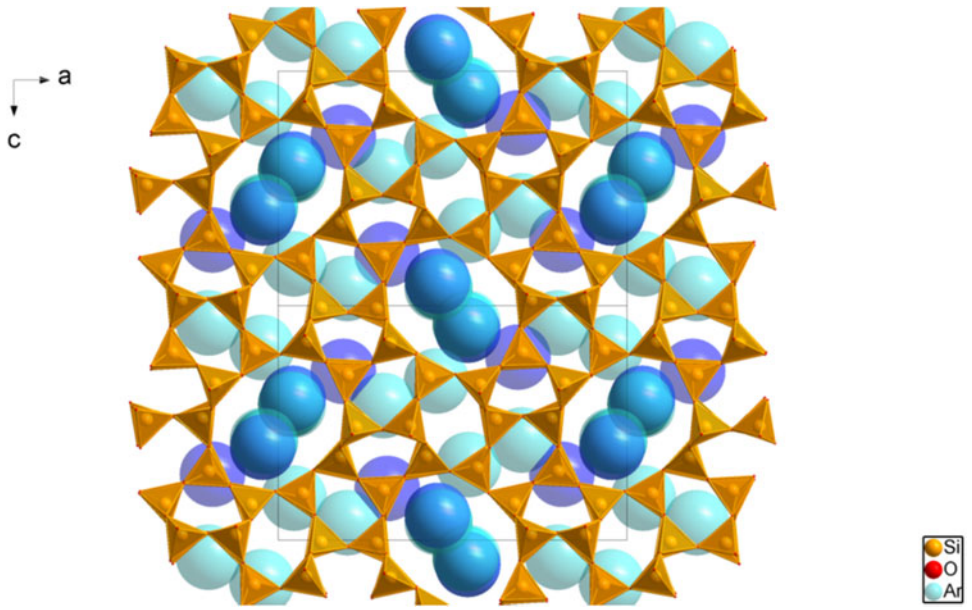

Figure 6. The crystal structure of Ar-filled MFI is viewed down the *b*-axis. Ar43 is colored blue, and Ar40 is in purple. The other Ar sites are colored cyan. Image generated using Diamond (Crystal Impact, 2022).

https://doi.org/10.1017/S0885715623000453 Published online by Cambridge University Press

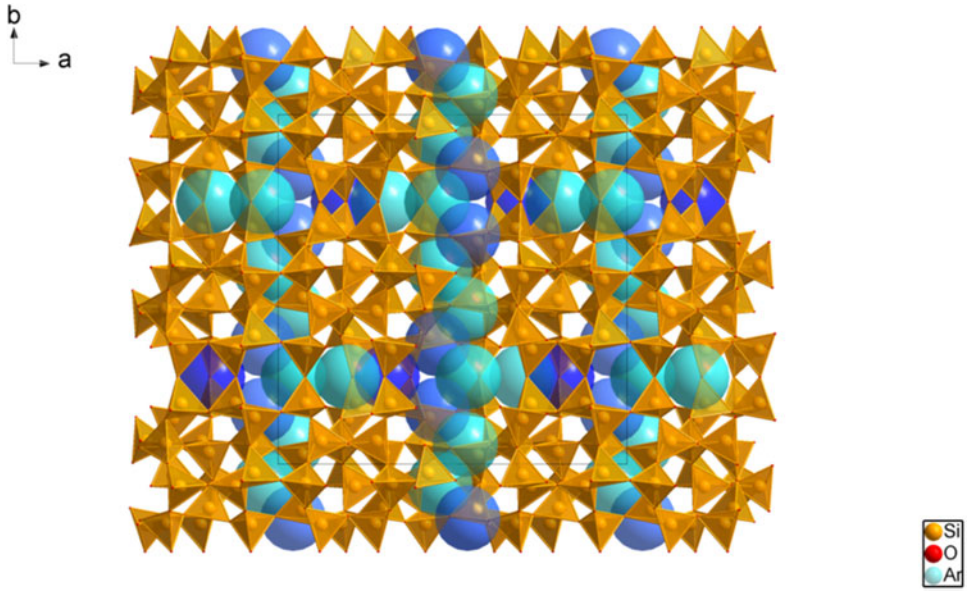

Figure 7. The crystal structure of Ar-filled MFI is viewed down the *c*-axis. Ar43 is colored blue, and Ar40 is in purple. The other Ar sites are colored cyan. Image generated using Diamond (Crystal Impact, 2022).

TABLE II. Shortest Ar–Ar and Ar–O distances (Å) in Ar-MFI at 90 K (run 11bmb_8192).

Site	Ar39	Ar40	Ar41	Ar42	Ar43	Ar44
Ar39				3.35(2)3.68(3) O35		
Ar40				3.01(2)3.27(3) O35		
Ar41			3.45(2)3.39(3) O18		3.52(2)	
Ar42	3.35(2)	3.01(2)3.56(3) O23				
Ar43			3.52(2)3.42(3) O13			3.52(1)3.46(3) O14
Ar44					3.52(2)3.52(3)O293.52(3) O31	

Top = Ar–Ar, bottom = Ar–O. Values inside brackets represent standard deviations.

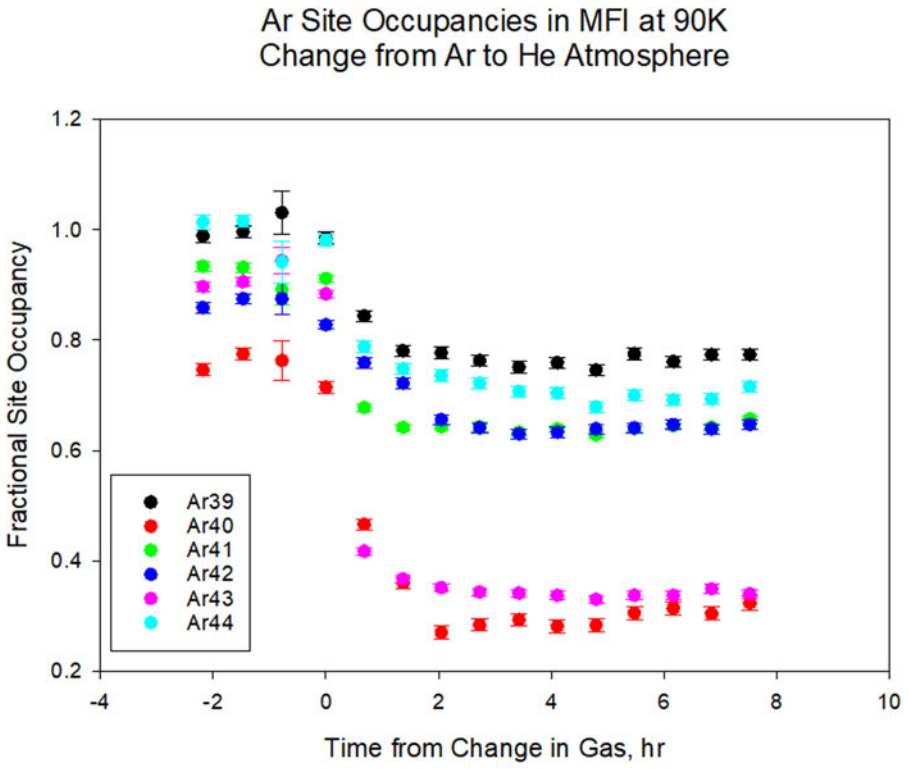

Figure 8. Ar site occupancies (uncertainty expressed as standard deviation) at 90 K in MFI as a function of time. The zero of time is the change from Ar to He atmosphere.

https://doi.org/10.1017/S0885715623000453 Published online by Cambridge University Press

TABLE III. Occupancy of Ar sites in MFI at different temperatures and gas compositions. Standard uncertainty = 0.01 for all values.

Site	Ar39	Ar40	Ar41	Ar42	Ar43	Ar44
90 K/Ar	1.00	0.76	0.92	0.87	0.91	0.99
90 K/He	0.77	0.32	0.66	0.65	0.34	0.32
295 K/Ar	0.51	0.00	0.38	0.46	0.32	0.38

TABLE IV. Absolute position differences (Å) for the Ar sites in the VASP-optimized fully occupied structure compared to the optimized structures with individual sites fully occupied.

Site	Ar39	Ar40	Ar41	Ar42	Ar43	Ar44
Δ, Å	0.320	0.412	1.153	0.783	0.751	0.578

2 h (Figure 8). The total Ar content decreased from 29 to 17 Ar/cell. The occupancies of Ar40 and Ar43 decreased more than the other four. Ar40 lies in the zig-zag channel and Ar43 lies in the straight channel. VASP calculations of individual sites show that 43 is the lowest energy, 41 next, and the other 4 comparable. The absolute differences in Ar positions in the VASP-optimized full structure and those with individual Ar sites are relatively small (Table IV).

Changing the gas flow from He at 90 K to Ar and warming to room temperature results in a decrease in the Ar site occupancies of five of the sites (the most stable Ar43 excepted) and causes the occupancy of Ar40 to vanish (Table III). The total Ar content decreased to 11 Ar/cell (Table IV).

IV. CONCLUSIONS

We have performed a complete structure analysis of $(NH_4)_{3.27}Al_{3.27}Si_{92.73}O_{192}(H_2O)_{26.7}$ (NIST reference material RM 8852) using powder diffraction at beamline 11-BM of APS (ANL). Our results clarified that the observation of a small peak during a TGA experiment with Ar indeed corresponds to the presence of a phase transition between orthorhombic and monoclinic. The Ar atoms partially fill both the straight and zig-zag channels. Using density functional theory calculations, the interaction of the Ar atoms among themselves and the framework thus seem to be van der Waals interactions. The overlap populations did not reveal any directional interactions between the Ar atoms and the framework. The ammonium cation lies in the zig-zag channels, between the straight channels. The ammonium ion does not seem to hydrogen bond to the framework, as the shortest N⋯O distances are 3.774 Å (to O33) and 3.805 Å (to O20). As is typical at ambient conditions, the water molecules have a high degree of disorder and they cannot be located with certainty.

V. DEPOSITED DATA

Selected powder patterns from this synchrotron study have been submitted to ICDD for inclusion in the Powder Diffraction File. The Crystallographic Information Framework (CIF) files containing the results of the Rietveld refinements (including the raw data) and the DFT geometry optimizations were deposited with the ICDD. The data can be requested at pdj@icdd.com.

ACKNOWLEDGEMENTS

Use of the Advanced Photon Source at Argonne National Laboratory was supported by the U. S. Department of Energy, Office of Science, Office of Basic Energy Sciences, under Contract No. DE-AC02-06CH11357. We thank Lynn Ribaud and Saul Lapidus for their assistance in the data collection.

CONFLICTS OF INTEREST

The authors have no conflicts of interest to declare.

REFERENCES

Antao, S. M., I. Hassan, J. Wang, P. L. Lee, and B. H. Toby. 2008. "State-of-the-Art High-Resolution Powder X-ray Diffraction (HRPXRD) Illustrated with Rietveld Refinement of Quartz, Sodalite, Tremolite, and Meionite." *Canadian Mineralogist* 46: 1501–9.

Artioli, G., C. Lamberti, and G. L. Marra. 2000. "Neutron Powder Diffraction Study of Orthorhombic and Monoclinic Defective Silicate." *Acta Crystallographica Section B: Structural Science* 56: 2–10.

Cho, H. S., K. Miyasaka, H. Kim, Y. Kubota, M. Takata, S. Kitagawa, R. Ryoo, and O. Terasaki. 2012. "Study of Argon Gas Adsorption in Ordered Mesoporous MFI Zeolite Framework." *The Journal of Physical Chemistry C* 116: 25300–8.

Crystal Impact. 2022. *Diamond. V. 4.6.8. Crystal Impact – Dr. H. Putz & Dr. K. Brandenburg*. Bonn, Windows.

Erba, A., J. K. Desmarais, S. Casassa, B. Civalleri, L. Donà, I. J. Bush, B. Searle, L. Maschio, L.-E. Daga, A. Cossard, C. Ribaldone, E. Ascrizzi, N. L. Marana, J.-P. Flament, and B. Kirtman. 2023. "CRYSTAL23: A Program for Computational Solid State Physics and Chemistry." *Journal of Chemical Theory and Computation* 19: 6891–6932. doi:10.1021/acs.jctc.2c00958.

Guesmi, H., P. Massiani, H. Nouali, and J.-L. Paillaud. 2012. "A Combined Experimental and Theoretical Study of the Simultaneous Occupation of Sia and Si' Sites in Fully Dehydrated K-LSX." *Microporous and Mesoporous Materials* 159: 87–95.

Heo, N. H., W. T. Lim, and K. Seff. 1996. "Crystal Structures of Encapsulates within Zeolites. 2. Argon in Zeolite A." *Journal of Physical Chemistry* 100: 13725–31.

Kresse, G., and J. Furthmüller. 1996. "Efficiency of Ab-Initio Total Energy Calculations for Metals and Semiconductors Using a Plane-Wave Basis Set." *Computational Materials Science* 6: 15–50.

Lee, P. L., D. Shu, M. Ramanathan, C. Preissner, J. Wang, M. A. Beno, R. B. Von Dreele, L. Ribaud, C. Kurtz, S. M. Antao, X. Jiao, and B. H. Toby. 2008. "A Twelve-Analyzer Detector System for High-Resolution Powder Diffraction." *Journal of Synchrotron Radiation* 15: 427–32.

Lee, Y., J. A. Hriljac, and T. Vogt. 2010. "Pressure-Induced Argon Insertion into an Auxetic Small Pore Zeolite." *Journal of Physical Chemistry C* 114: 6922–7.

Macrae, C. F., I. Sovago, S. J. Cottrell, P. T. A. Galek, P. McCabe, E. Pidcock, M. Platings, G. P. Shields, J. S. Stevens, M. Towler, and P. A. Wood. 2020. "*Mercury 4.0*: From Visualization to Design and Prediction." *Journal of Applied Crystallography* 53: 226–35.

Materials Design. 2016. *MedeA 2.20.4*. Angel Fire, NM, Materials Design Inc.

MDI. 2023. *JADE Pro Version 8.8*. Livermore, CA, Materials Data.

Nguyen, H. G. T., L. Espinal, R. D. van Zee, M. Thommes, B. Toman, M. S. L. Hudson, and G. De Weireld. 2018. "A Reference High-Pressure CO_2 Adsorption Isotherm for Ammonium ZSM-5 Zeolite: Results of an Interlaboratory Study." *Adsorption* 24 (6): 531–9. doi:10.1007/s10450-018-9958-x.

Nguyen, H. G. T., B. Toman, J. Colon Martinez, D. W. Siderius, and R. D. van Zee. 2022. "Reference Surface Excess Isotherms for Carbon Dioxide

Adsorption on Ammonium ZSM-5 at Various Temperatures." *Adsorption* 28: 15–25. doi:10.1007/s10450-022-00355-x.

Stephens, P. W. 1999. "Phenomenological Model of Anisotropic Peak Broadening in Powder Diffraction." *Journal of Applied Crystallography* 32: 281–9.

Toby, B. H., and R. B. Von Dreele. 2013. "GSAS II: The Genesis of a Modern Open Source All Purpose Crystallography Software Package." *Journal of Applied Crystallography* 46: 544–9.

Turner, S., J. R. Sieber, T. W. Vetter, R. Zeisler, A. F. Marlow, M. G. Moreno-Ramirez, M. E. Davis, G. J. Kennedy, W. G. Borghard, S. Yang, A. Navrotsky, B. H. Toby, J. F. Kelly, R. A. Fletcher, E. S. Windsor, J. R. Verkouteren, and S. D. Leigh. 2008. "Characterization of Chemical Properties, Unit Cell Parameters and Particle Size Distribution of Three Zeolite Reference Materials: RM 8850 – Zeolite Y, RM 8851 – Zeolite A and RM 8852 – Ammonium ZSM-5 Zeolite." *Microporous and Mesoporous Materials* 107: 252–67.

van de Streek, J., and M. A. Neumann. 2014. "Validation of Molecular Crystal Structures from Powder Diffraction Data with Dispersion-Corrected Density Functional Theory (DFT-D)." *Acta Crystallographica Section B: Structural Science, Crystal Engineering and Materials* 70: 1020–32.

Wang, J., B. H. Toby, P. L. Lee, L. Ribaud, S. M. Antao, C. Kurtz, M. Ramanathan, R. B. Von Dreele, and M. A. Beno. 2008. "A Dedicated Powder Diffraction Beamline at the Advanced Photon Source: Commissioning and Early Operational Results." *Review of Scientific Instruments* 79: 085105.

https://doi.org/10.1017/S0885715623000453 Published online by Cambridge University Press